# Comparison of the Bouguer reduction approach for the satellite gravity data: Case study of the eastern Tibetan Plateau and its adjacent areas

*Fan Luo[1,2,3], Jiayong Yan[2,3], Kun Zhang[2,3], Chong Zhang[2,3], Guangming Fu[1,2,3] and Xin Tao[1,2,3]*

[1] School of Geophysics and Measurement Control Technology, East China University of Technology, Nanchang, China

[2] Chinese Academy of Geological Sciences, Beijing, China

[3] China Deep Exploration Center, China Geological Survey and Chinese Academy of Geological Sciences, Beijing, China

Satellite gravity data are widely used in the field of geophysics to study deep structures at the regional and global scales. These data comprise free-air gravity anomaly data, which usually need to be corrected to a Bouguer gravity anomaly for practical application. Bouguer reduction approaches can be divided into two methods based on the coordinate system: the spherical coordinates method (SBG) and the Cartesian coordinates method; the latter is further divided into the CEBG and CBG methods, which do and do not include the Earth's curvature correction. In this paper, free-air gravity anomaly data from the eastern Tibetan Plateau and its adjacent areas were used as the basic data to compare the CBG, CEBG, and SBG Bouguer gravity correction methods. The comparison of these three Bouguer gravity correction methods shows that the effect of the Earth's curvature on the gravitational effect increases with increasing elevation in the study area. We want to understand the inversion accuracy for the data obtained by different Bouguer gravity reduction approaches. The depth distributions of the Moho were obtained by the interface inversion of the Bouguer gravity anomalies obtained by the CBG, CEBG, and SBG, and active seismic profiles were used as references for comparison and evaluation. The results show that the depths of the Moho obtained by the SBG inversion are more consistent with the measured seismic profile depths. Therefore, the SBG method is recommended as the most realistic approach in the process of global or regional research employing gravity data.

*Keywords*: Bouguer reduction approach, spherical coordinates, Moho surface, eastern Tibetan Plateau and its adjacent areas

# 1. Introduction

The gravity method is an essential component of geophysical exploration. Reductions are needed according to the purpose of the research to obtain the corresponding gravity anomaly before implementing the gravity data. The Bouguer gravity anomaly is one of the most widely used gravity anomalies that includes reductions such as the free-air correction and Bouguer correction from raw gravity data (Hofmann-Wellenhof and Moritz, 2006). The correction obtained using the free-air gravity formula proposed by Lambert and Hesiskanen can be calculated accurately as a free-air gravity anomaly (Lambert, 1930; Hesiskanen and Moritz, 1967). The Bouguer gravity reduction is divided into three separate steps: (1) Bouguer plate correction, (2) Earth's curvature correction, and (3) terrain correction (Bullard, 1936). The study area is approximated as a plane, and the effect of the Earth's curvature on the gravity signal is easy to ignore; hence, the Bouguer gravity anomaly can be calculated quickly in the early stage of applying the Bouguer gravity reduction. A Bouguer correction approach to calculate the Bouguer gravity correction within 1.5° (~ 167 km) is widely used to calculate the Bouguer gravity anomaly based on the terrain in the Cartesian coordinate system and the Bouguer plate formula (Hayford and Bowie, 1912; Nagy, 1966; Kane, 1962). The threshold for the horizontal range of the study area is 200 km, if the horizontal scale is less than 200 km, the effect of the Earth's curvature on gravity can be ignored in the calculation of the Bouguer reduction (Li et al., 2011); vice versa, the influence of the Earth's curvature on gravity must be considered if the horizontal extent is greater than 200 km. LaFehr proposed an accurate expression for the Earth's curvature correction in 1990 (LaFehr, 1990). Subsequently, Whitman (1991) simplified LaFehr's formula while ensuring accuracy. Fullea (2008) calculated Bouguer corrections within a range of 167 km while including the effect of the Earth's curvature in the Cartesian coordinate system based on the calculation steps (Bullard, 1936) and formulas (LaFehr, 1990; Nagy, 2000) of the Bouguer gravity correction. In another method used to consider the Earth's curvature, the Bouguer gravity correction is approximated, by regarding the Earth as a sphere and then calculating the Bouguer gravity corrections in the spherical coordinate system. LaFehr (1990), Mikuška et al. (2006), and Grombein (2013) deduced the analytic expressions of the gravitational field of a tesseroid unit cell in the spherical coordinate system and defined the necessary conditions for the existence of an analytic solution. Wild-Pfeiffer (2008) and Uield (2016) studied an adaptive calculation method to calculate the gravity effect of a body in the tesseroid model in the spherical coordinate system. The Bouguer gravity correction approach requires different calculation steps between the spherical coordinate system and the Cartesian coordinate system. A combination of the Bouguer plate correction and the terrain correction is needed to calculate Bouguer gravity corrections in the spherical coordinate system (An et al., 2010).

Gravity data can be divided into four categories according to the different means of obtaining observations: ground surveys, ship surveys, aerial surveys, and satellite surveys. The first satellite altimeter to observe gravity was launched in the 1980s (Haxby, 1985). With several phase of development in satellites and instrumentation technology spanning nearly four decades, the resolution and accuracy of satellite altimetry/gravity datasets have been significantly improved following the implementation of a series of professional gravity satellite measuring programmes (including GRACE, GOCE, and CHAMP) and the addition of repeat mission data (Geosat, ERS-1, Topex/Poseidon, etc.) (Cheney et al., 1987; Rignot and Van, 1993; Fu et al., 1994; Green et al., 2019). Notwithstanding the above upgrades, the orbits of satellite platforms are located between 250 and 500 km above the surface, which limits the spatial resolution and accuracy of the surface and subsurface gravity anomalies measured at such orbital heights (Green et al., 2019). To obtain gravity data with greater accuracy, satellite and terrestrial data were integrated based on gravity potential theory. This resulted in the construction of a series of approximate real gravity field expressions to satisfy the high precision and resolution requirements in the global gravity field model (EIGEN-6C4, EGM2008, GOCO01S, etc.) (Pavlis et al., 2012; Förste et al., 2014; Pail et al., 2010). Many scholars use gravity data calculated by the global gravity field model as the basis and combine these data with geological data while investigating deep underground conditions at the regional and global scales to provide critical constraints for research on the Earth's deep structure and dynamics (Pappa et al., 2019; Rathnayake et al., 2019; Pastorutti and Braitenberg, 2019).

Satellite gravity data, which belongs to the category of gravity data, are calculated based on the global gravity field model so a series of corrections are needed to obtain and apply Bouguer gravity anomalies. According to the above introduction to the development of the Bouguer reduction method, the reduction approach can be divided into two categories based on the coordinate system, namely, the Cartesian coordinate system (comprising two cases, that is, whether the Earth's curvature is considered) and the spherical coordinate system. The Bouguer gravity reduction methods described above are widely used in the correction of satellite gravity data (Vaish and Pal, 2015; Pal and Majumdar, 2015; Tamay et al., 2018; Almalki and Mahmud, 2018; Maurya et al., 2017; Mahatsente et al., 2018; Peters et al., 2018; Zhu and Li, 2018; Chen et al., 2018; Sobh et al., 2018; Deng and Shen, 2019; Zhao et al., 2019). Most relevant satellite gravity data studies select one of these two reduction approaches for practical applications. However, no comparative analysis of the Bouguer gravity anomaly data obtained by different Bouguer reduction approaches has been conducted. Therefore, in this paper, we compare and analyse the difference in Bouguer gravity anomaly data obtained by correcting satellite gravity data with the different Bouguer gravity reduction approaches described above to reveal which Bouguer reduction approach is the most suitable for actual situations.

## 2. Method and principle

The Bouguer reduction approach can be divided into two categories based on the coordinate system employed, namely, the Cartesian coordinate system (comprising two cases, that is, whether the Earth's curvature is considered) and the spherical coordinate system. Each of these components will be described in the following to show how the Bouguer gravity reduction technique works in the Cartesian and spherical coordinate systems.

### 2.1. Bouguer gravity reduction approach in the Cartesian coordinate system

The Bouguer gravity reduction in the Cartesian coordinate system is divided into three separate steps: (1) Bouguer plate correction, (2) Earth's curvature correction, (3) terrain correction (Bullard, 1936).

#### 2.1.1. Bouguer plate correction

The area of gravity point $P$ is assumed to be an entirely horizontal plane (Fig. 1), and between the geoid and the Earth's surface, the volume density is constant. Then, the calculation formula of the Bouguer plate is as follows (Hofmann-Wellenhof and Moritz, 2006):

$$A_B = 2\pi G\rho h \ . \tag{1}$$

Here, $G$ represents the gravitational constant; $\rho$ represents the density, and $h$ represents elevation.

This expression for calculating the influence of gravity on the Bouguer plate needs to comprehensively consider different conditions in both continental and oceanic regions. Then, the calculation formula of the influence of gravity in the Bouguer plate is as follows (Uield et al., 2016):

$$\Delta g_B = -0.0419088 \cdot \left[ \rho_c h_s + (\rho_w - \rho_c)h_w \right]. \tag{2}$$

Here, $\Delta g_B$ indicates the result of the Bouguer plate (unit: mGal); $\rho_c$ and $\rho_w$ represent the density of continental and oceanic regions, respectively, (unit: kg/m$^3$); and $h_s$, and $h_w$ represent the elevation in continental and oceanic regions, respectively (unit: m).
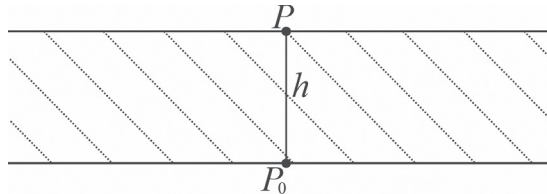


**Figure 1.** Bouguer plate.

### *2.1.2. Terrain correction*

The correction for the difference between the Bouguer plate and the actual topography of the Earth's surface is called the terrain correction. In the terrain correction process, in a region with a mass surplus (A), the gravity direction is upward, and thus, this residual mass needs to be removed. In a region with a mass deficiency (B), the gravity direction is downward, and thus, this mass deficiency needs to be filled (Fig. 2). Therefore, the terrain correction is always positive (Hoftmann and Moritz, 2006), to balance the calculation efficiency and accuracy in the terrain correction process. According to the distance from the gravity measurement point and the gravity measurement point as the centre, the terrain correction is divided into three concentric square areas; the near zone (0 ~ 2 km), the medium zone (2 ~ 20 km), and the far zone (20 ~ 167 km) (Fig. 3). Different regions use different formulas for the calculation.

The terrain correction values in adjacent areas are obtained by calculating the gravitational effect of four oblique triangles formed by the calculation points, and the surrounding four measurement points. The calculation formula is as follows:

$$\Delta g_{t_1} = G\rho\phi\left( R - \sqrt{R^2 + H^2} + \frac{H^2}{\sqrt{R^2 + H^2}} \right). \tag{3}$$

Here, $\Delta g_{t_1}$. indicates the resulting of the terrain correction value in an adjacent area (unit: mGal); $G$ represents the gravitational constant; $\rho$ represents the density; $R$ represents the projected distance between two adjacent gravity measurement points; $H$ represents the terrain point elevation; and $\phi$ represents the angle between the projection of two nearby terrain points and the calculated point.
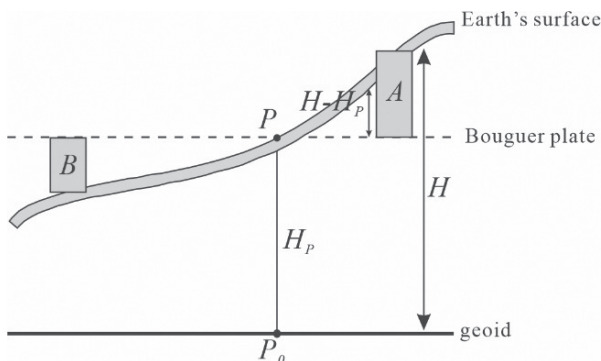


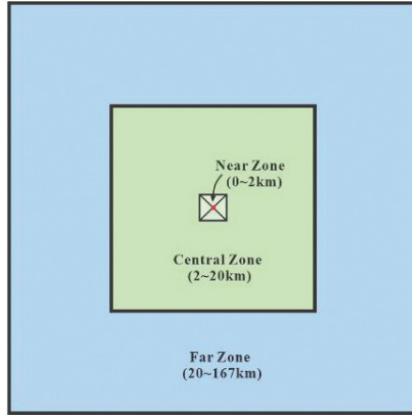**Figure 2.** Terrain correction.

**Figure 3.** Different computational zones according to the distance between the terrain and calculation point.

The formula for calculating the gravitational effect of a semi-infinite prism body at the point $P(0,0,z)$ in the middle zone is as follows (Nagy, 1966, 2000):

$$\Delta g_{t_2} = G\rho z \left( p \cdot \log \frac{q+r}{\sqrt{1+p^2}} + q \cdot \log \frac{p+r}{\sqrt{1+q^2}} - \arctan \frac{p \cdot q}{r} \right),$$

(4)

$$p = \frac{q}{z}, q = \frac{y}{z}, r = \sqrt{1+p^2+q^2} .$$

Here, $\Delta g_{t_2}$ indicates the resulting terrain correction value in the middle zone, $G$ represents the gravitational constant, $\rho$ represents the density, and $x$, $y$ represent the coordinates of the top point of the prism.

The calculation formula for the terrain correction value in the far zone is as follows (Kane, 1962):

$$\Delta g_{t_3} = 2G\rho A^2 \frac{\left( R_2 - R_1 \sqrt{R_1^2 + H^2} - \sqrt{R_2^2 + H^2} \right)}{R_2^2 + R_1^2} .$$

(5)

Here, $\Delta g_{t_3}$ indicates the resulting terrain correction value in the far zone, $G$ represents the gravitational constant; $\rho$ represents the density, $A$ represents the length of the horizontal side of the prism, $R_1$ and $R_2$ represent the inside and outside radius, respectively, and $H$ represents elevation.

The terrain correction values calculated for the near (3), middle (4), and far (5) zones are combined to obtain the terrain correction value for the gravity measurement point:

$$\Delta g_{tc} = \Delta g_{t_1} + \Delta g_{t_2} + \Delta g_{t_3}.$$

(6)

Here, $\Delta g_{tc}$ indicates the resulting terrain correction value and $\Delta g_{t_1}$, $\Delta g_{t_2}$, and $\Delta g_{t_3}$ represent the resulting terrain correction values in the near, middle, and far zones, respectively.

### 2.1.3. Earth's curvature correction

The Earth's curvature or degree of curvature earth is usually expressed by the radius of curvature or by the curvature (that is, the inverse of the radius of curvature). The Earth's curvature affects the measurement of elevation, and therefore, the influence of the Earth's curvature on gravity should be considered in addition to the Bouguer plate and terrain correction in high precision Bouguer gravity corrections (Whitman, 1991).

The formula for the Earth's curvature correction is as follows (Swick, 1942; LaFehr, 1991):

– If $h > 0$, then

$$BB = -2\pi G \rho_c h \left( \frac{\alpha}{2} - \frac{\eta}{2\alpha} - \eta \right), \tag{7}$$

– If $h < 0$, then

$$BB = -2\pi G (\rho_c - \rho_w) h \left( \frac{\alpha}{2} - \frac{\eta}{2\alpha} - \eta \right), \tag{8}$$

where $\alpha = R_d / R_T, \eta = h / (R_T + h)$. Here, $R_T$ represents the radius of a spherical Earth (unit: km), $R_d$ is the radius to a distant zone (unit: km), $G$ represents the gravitational constant, $\rho_c$ represents the land area reduction density (unit: kg/m$^3$), $\rho_w$ represents the water area reduction density (unit: kg/m$^3$), and $h$ represents the elevation (unit: m).

In summary, the expression for calculating the complete Bouguer gravity anomaly in the Cartesian coordinate system can be expressed as follows:

$$\Delta g_{CB} = \Delta g_{FA} + \Delta g_B + \Delta g_{tc} + BB . \tag{9}$$

Here, $\Delta g_{CB}$ indicates the result of the complete Bouguer gravity anomaly, $\Delta g_{FA}$ represents the free-air gravity anomaly, $\Delta g_B$ represents the result of the Bouguer plate correction, $\Delta g_{tc}$ represents the result of the terrain correction, and $BB$ represents the result of the Earth's curvature correction.

### 2.2. Bouguer gravity reduction approach in the spherical coordinate system

Another way to find the Bouguer gravity anomaly is to approximate the Earth as a sphere, and then calculate the Bouguer gravity anomaly in the spherical coordinate system. A common method for obtaining Bouguer corrections in a spherical coordinate system is to discretize the Earth into a tesseroid unit model (Fig. 4) rather than a rectangular prism model (Uield et al., 2016). The

procedure for calculating the Bouguer correction based on the a tesseroid body in the spherical coordinate system is different from the procedure of Bullard (1936) in a flat rectangular coordinate system. The former is directly combined with the Bouguer plate correction and terrain correction for a calculation without separation. LaFehr (1990), Mikuška et al. (2006), and Grombein (2013) deduced analytic expressions of the gravitational field of a tesseroid cell in the spherical coordinate system and defined the necessary conditions for the existence of an analytic solution. The method used to numerically integrate of the tesseroid model usually adopts the Taylor series expansion (Heck and Seitz, 2007; Grombein et al., 2013) or the Gauss-Legendre Quadrature (GLQ) function (Asgharzadeh et al., 2007). The Taylor series expansion method will reduce the calculation accuracy at low latitudes, while the GLQ method uses the number of mass points to control the calculation accuracy, and the larger the number of mass points is, the higher the accuracy of the GLQ method (Uield et al., 2016). Therefore, this article uses the GLQ method to calculate the gravity value of in the tesseroid model.
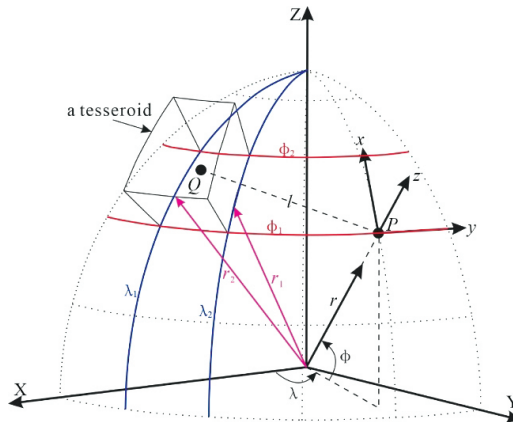


**Figure 4.** View of a tesseroid. Point *P* represents the computation point in the local coordinate system; the point *Q* represents the integration point in the geocentric coordinate system; $r, \phi, \lambda$ are the radius, latitude, and longitude, respectively, and l represents the distance between *P* and *Q*.

The gravity field formula of the tesseroid model is shown as follows (Grombein et al., 2013):

$$g_\alpha(r,\phi,\lambda) = G\rho \int_{\lambda_1}^{\lambda_2}\int_{\phi_1}^{\phi_2}\int_{r_1}^{r_2} \frac{\Delta_\alpha}{l^3} K dr' d\phi' d\lambda' \qquad (10)$$

Here, $\alpha, \beta \in \{x, y, z\}$; $\rho$ represents the density; $G$ represents the gravita-tional constant; $\delta_{\alpha,\beta}$ represents Kronecker's delta (if $\alpha = \beta$, then $\delta_{\alpha,\beta} = 1$; if $\alpha \neq \beta$, then $\delta_{\alpha,\beta} = 0$); and

$$\Delta_x = r'\big(\cos\phi\sin\phi' - \sin\phi'\cos\phi'\cos(\lambda' - \lambda)\big)$$

$$\Delta_y = r'\cos\phi'\sin(\lambda' - \lambda)$$

$$\Delta_z = r'\cos\psi - r$$

$$\kappa = r'^2\cos\phi'$$

$$l = \sqrt{r'^2 + r^2 - 2r'r\cos\phi}$$

$$\cos\psi = \sin\phi\sin\phi' - \cos\phi'\cos\phi'\cos(\lambda' - \lambda).$$

The tesseroid model performs the numerical integration using the GLQ function for 3D volume integrals; the equation is (Asgharzadeh et al., 2007).

$$\Delta g_{impact} = \iiint_\Omega f(r', \lambda', \phi')d\Omega \approx A \sum_{i=1}^{N^r} \sum_{j=1}^{N^\phi} \sum_{k=1}^{N^\lambda} W_i^r W_j^\varphi W_k^\lambda f(r_i, \lambda_j, \phi_k), \qquad (11)$$

$$A = \frac{(\lambda_2 - \lambda_1)(\phi_2 - \varphi_1)(r_2 - r_1)}{8},$$

where $W_i^r$, $W_j^\varphi$, and $W_k^\lambda$ represent the weight coefficients, and $N^r$, $N^\varphi$, and $N^\lambda$ represent the integral node data.

The tesseroid model is applied to the free-air anomaly to obtain the Bouguer anomaly using the following equation:

$$\Delta g_B = \Delta g_{FA} - \Delta g_{impact}. \qquad (12)$$

Here, $\Delta g_B$ indicates the result of the Bouguer gravity anomaly, $\Delta g_{FA}$ represents the free-air gravity anomaly, and $\Delta g_{impact}$ represents the resulting gravity value.

## 3. Study area and datasets

The eastern Tibetan Plateau and its adjacent areas (between the latitudes 18° N and 44° N and between the longitudes 88° E and 114° E) are located in southwestern China. This area has long been affected by the collision between the Indian plate and the Eurasian plate, causing strong tectonic deformation (Xu et al., 2018). The northeastern part of the study area is mainly composed of the Ordos Plain, Alashan Desert, and Northeast Asia plate; the northwestern is the Tibetan Plateau, Tarim Basin, and Junggar Basin; the central part consists of the Songpan-Ganzi terrane, Chuandian Plateau, Sichuan Basin, Qaidam Basin,
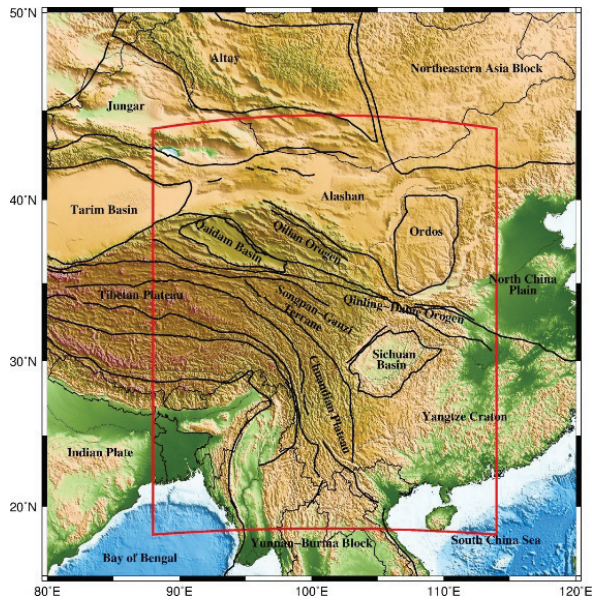
**Figure 5.** Map of the eastern Tibetan Plateau and its adjacent areas with major tectonic features; the red solid rectangule shows the location of the study area.

Qinling-Dabie orogen, and Qilian orogenic belt; the southwestern and southeastern areas are the Indian Plate and Yangtze craton, respectively (Fig. 5) (Xu et al., 2013). The study area includes a variety of landforms such as plateaus, basins, deserts, and plains, with significant topographical differences and a wide range of research areas. Hence, this region is an ideal area to study the differences between different Bouguer reduction methods. Therefore, this article uses the eastern Tibetan Plateau and its adjacent areas as the research area.

The satellite gravity data we used in this study are from the EIGEN-6C4 global gravitational model (Förste et al., 2014), and the ETOPO1 topography, ocean bathymetry, and glacial bedrock relief datasets (Amante and Eakins, 2009) are employed as topographic data.

The EIGEN-6C4 (EIGEN: European Improved Gravity model of the Earth by New techniques) gravity model is used to establish raw gravity value maps for the study area. The gravity data from the EIGEN-6C4 gravity model are reconstructed of from the Earth Gravity Model 2008 (EGM 2008) and are combined with data from the Laser GEO-dynamic Satellite (LAGEOS), Gravity Recovery and Climate Experiment (GRACE) mission and Gravity Field and steady-state Ocean Circulation Explorer Gravity (GOCE) satellite, which have been further augmented with the Danmarks Tekniske Universitet 10 ground data and have a spherical harmonics degree of 2,190. The spatial resolution of the EIGEN-6C4 model is ~ 9 km. The EIGEN-6C4 data are downloaded from the
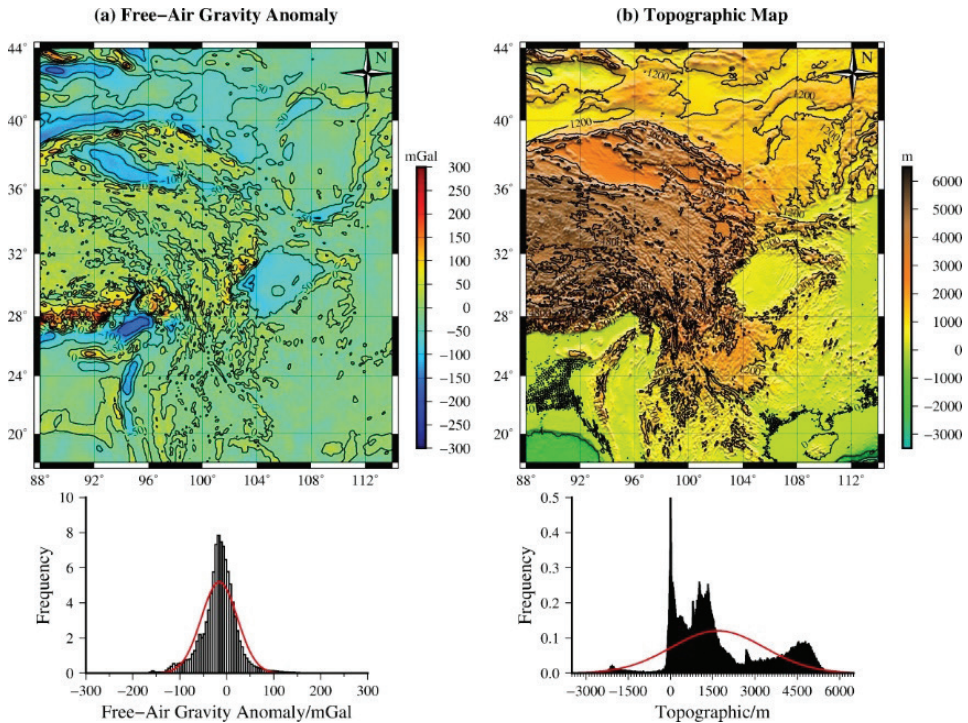
**Figure 6.** Map and histograms of the base data for the eastern Tibetan Plateau and adjacent areas. Left: free-air gravity anomaly data from the EIGEN-6C4 dataset (*a*); Right: topographic data from the ETOPO1 dataset (*b*).

website populating the "International Center for Global Earth Models" data (Barthelmes and Köhler, 2016; Drewes et al., 2016) and have already been widely used for subsurface structural research at the regional and global scales (Rani et al., 2019; Rathnayake et al., 2019, Rathnayake and Tenzer, 2019; Emishaw and Abdelsalam, 2019). The free-air gravity anomaly data employed as the basic data for this study have a resolution of 0.05° × 0.05° and are obtained from the ICGEM official website (http://icgem.gfz-potsdam.de/home). The free-air gravity anomalies along the eastern margin of the Tibetan Plateau and its adjacent areas range from – 300 to 300 mGal and from –100 to 100 mGal in most of the other areas. The low-value free-air gravity anomalies roughly correspond to basin (such as the Sichuan Basin and Qaidam Basin), while the high-value areas roughly correspond to the boundaries between the plateau and other landforms (Fig. 6a).

The ETOPO1 (Earth Topography One Arc-Minute Global Relief Model) datasets comprises the combination of shoreline, bathymetric, topographic, integrated bathymetric-topographic, and bedrock digital data sets. ETOPO1 data

are used as the terrain data for the study area. ETOPO1 data are reconstruct by data from the National Geophysical Data Center (NGDC) combined with data from United States government agencies, international agencies, and academic institutions. ETOPO1 provides topographic and bathymetric coverage between −90° and +90° latitude and between −180° and +180° longitude, and the data are downloaded from the website populating the "National Oceanic and Atmospheric Administration" database (https://data.nodc.noaa.gov/) (Amante and Eakins, 2009). The topographic data for the eastern Tibetan Plateau and its adjacent areas are derived from the ETOPO1 dataset (Fig. 6b), and the resolution is consistent with the resolution of the free-air gravity anomaly data, that is, 0.05° × 0.05°. The elevation data for the study area vary between approximately −3,500 and 6,500 m, and the elevation of most areas is concentrated in the range of 0 ~ 5,000 m.

## 4. Differences in the Bouguer reduction approaches

In this paper, the eastern Tibetan Plateau and its adjacent areas are selected as the study area, and the different Bouguer reduction approaches in the Cartesian coordinate system and spherical coordinate system mentioned above are compared and studied. These comparative analyses are divided mainly into the following three categories. First, the influence of the Earth's curvature on the Bouguer correction is studied by comparing the results of two cases in the Cartesian coordinate system together with the Earth's curvature. Second, the effects of different reduction methods on the Bouguer correction are studied by comparing the results of the Bouguer correction methods in the spherical coordinate system with those in the Cartesian coordinate system that includes the Earth's curvature correction. Finally, the correction results of different Bouguer reduction methods are inverted by the same method; then, the inverted depths of the Moho obtained by different Bouguer correction methods are evaluated with reference to the results of active seismic methods. The comparisons of the different Bouguer correction methods are described below.

### 4.1. Influence of the Earth's curvature in the Cartesian coordinate system

The free-air gravity anomalies in the eastern Tibetan Plateau and its adjacent areas (Fig. 6a) were corrected based on the different Bouguer correction methods in the Cartesian coordinate system. The difference between the Bouguer correction methods in the Cartesian coordinate system is only whether the Earth's curvature correction is considered. Therefore, the Bouguer correction method that considers the Earth's curvature correction in the Cartesian coordinate system is referred to as CEBG, while the method that does not consider the Earth's curvature correction is referred to as CBG. During the calibration process, the calibration parameters are set as follows: the calibration range is
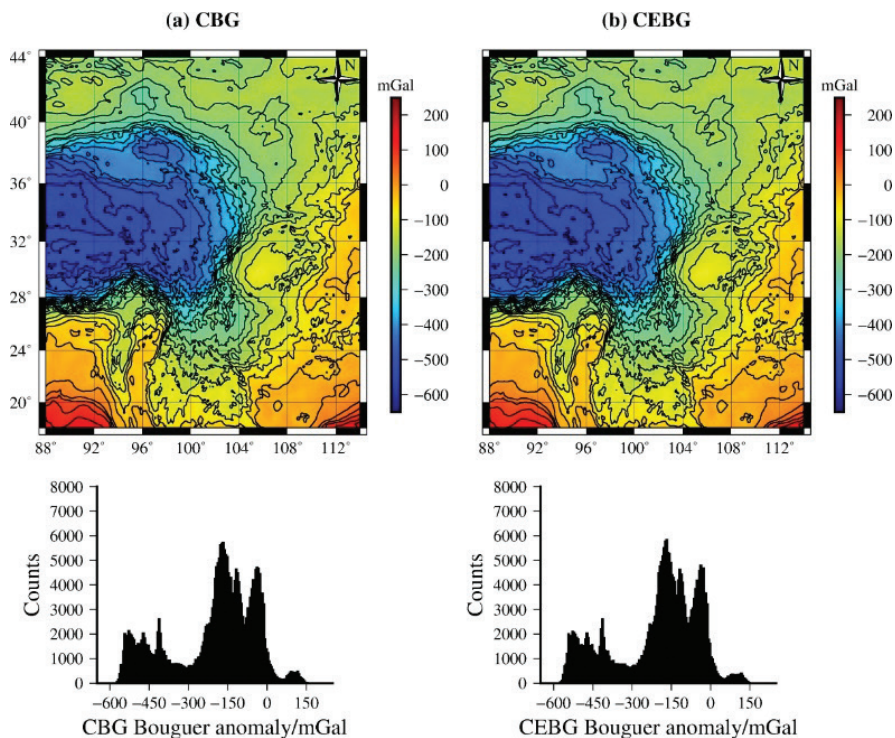
**Figure 7.** Map and histograms of the eastern Tibetan Plateau and adjacent areas of the Bouguer gravity anomaly. Left: CBG method (*a*); Right: CEBG method (*b*).

167 km, and the densities of the continent and ocean are 2,670 kg/m$^3$ and 1,000 kg/m$^3$, respectively.

The two Bouguer correction methods (CBG and CEBG) are used to obtained the Bouguer gravity anomalies in the study area, and the Bouguer gravity anomalies of both vary between – 650 and 150 mGal (Fig. 7). The same colour bar was used to graphically display the resulting Bouguer gravity anomalies. The maps show consistent distribution data, and the overall trend is that negative anomalies are in the continental area, while positive anomalies are in the ocean.

To further determine whether the influence of the Earth's curvature correction on the Bouguer gravity anomaly is taken into account in the Cartesian coordinate system, the Bouguer gravity anomalies obtained by CBG and CEBG methods were collected to obtain the residuals (Fig. 8a), and the residuals were processed as absolute values (Fig. 8b). The overall distribution of the difference between the Bouguer gravity anomalies obtained by the CBG and CEBG methods is shown in Figure 8a, and the difference in the anomalies varies between approximately 15 mGal and – 20 mGal. According to the data histogram in Fig. 8a, the numerical difference in most areas of the study region is mainly concen-
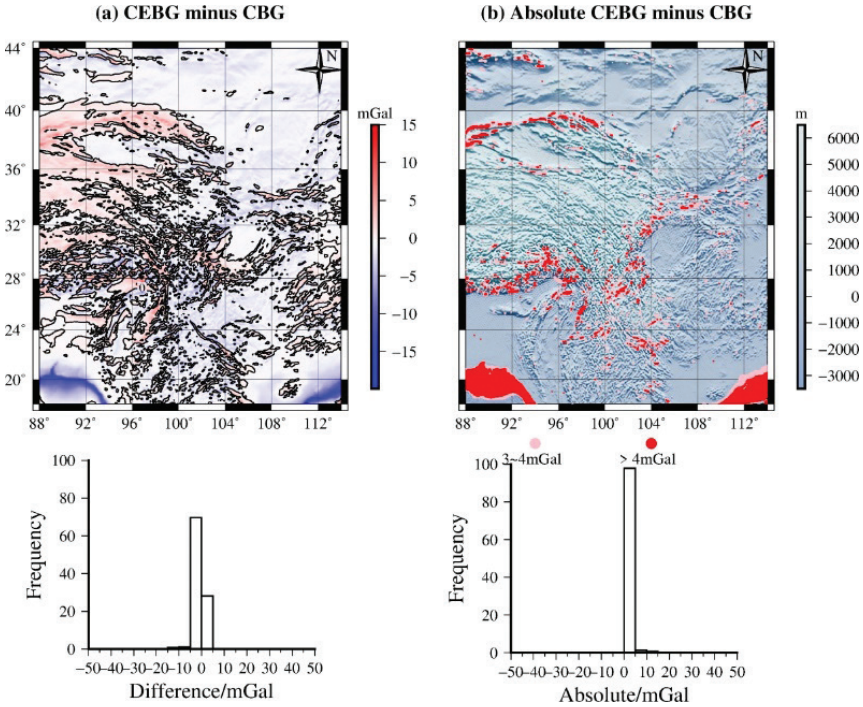
**Figure 8.** Differences between CBG and CEBG methods. Left: CEBG minus CBG (*a*); Right: absolute CEBG minus CBG (*b*).

trated between – 5 mGal and 5 mGal. The absolute residual values of the Bouguer gravity anomaly were extracted from the CBG and CEBG methods, and pink and red points were used to represent anomalies of 3 ~ 4 mGal and above 4 mGal, respectively, and then marked on the topographic map (Fig. 8b). The pink and red points are mainly distributed in the boundary areas between the Tibetan Plateau and the surrounding basins, as well as the boundary areas between the continent and the ocean. Based on Figs. 7 and 8, in the study range of 26°×26°, the influence of the Earth's curvature on the gravitational effect is distributed across the whole region, and the influence is particularly severe in the regions with significant terrain.

### 4.2. Comparison between the Bouguer correction methods in the Cartesian coordinate system and spherical coordinate system

The Bouguer gravity reduction methods of in the Cartesian coordinate system mentioned above are all based on the reduction of the Cartesian coordinate system. The Bouguer reduction methods in the Cartesian coordinate system with the Earth's curvature correction simply convert the Bouguer plate correction to

the Bouguer correction with curvature, but the effect of the Earth's curvature is not considered in the terrain correction. The degrees of curvature of different areas of on the Earth's surface is differ. Therefore, it is most realistic to take the exact shape of the Earth (ellipsoid) as the reference coordinate system for the correction. However, the calculation of the gravitational effect in the ellipsoidal coordinate system is complicated, and the number of calculations is enormous. Therefore, the Earth is usually approximated as a sphere, and the gravitational effect is calculated in the spherical coordinate system. The Bouguer gravity correction method for free-air gravity anomalies in spherical coordinates has been described in the principles section above; this method is referred to as SBG in this paper. During the correction process, the free-air gravity anomaly data, terrain data, and correction parameters used are consistent with the parameters employed for the Bouguer gravity reduction method considering the Earth's curvature in the Cartesian coordinate system, which facilitates a comparison between the CEBG and SBG methods.

Figures 9 (a) and (b) show the Bouguer gravity anomalies obtained by the CEBG and SBG correction methods, respectively, on the eastern Tibetan Plateau
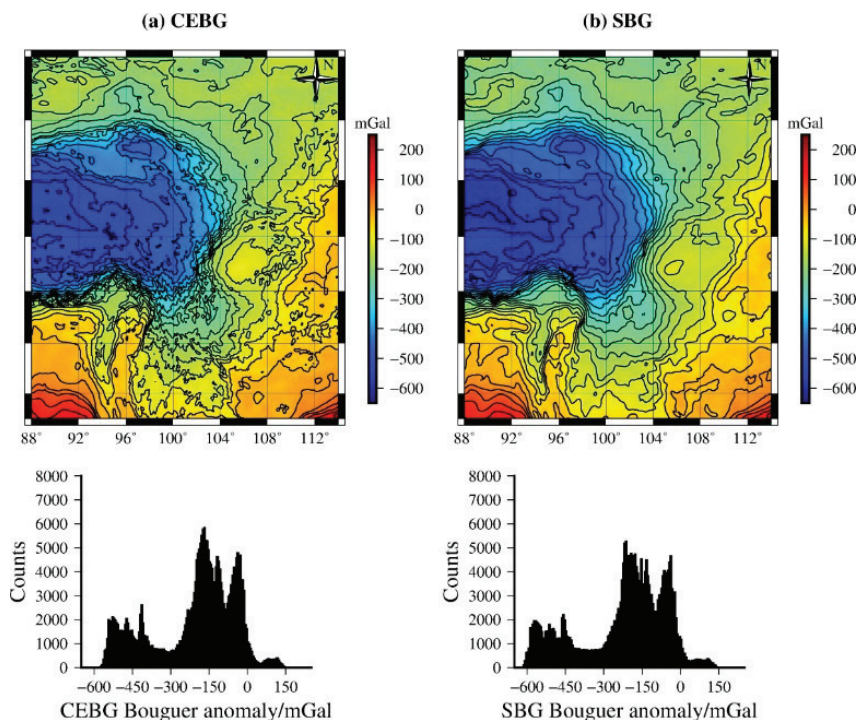


**Figure 9.** Map and histograms of the Bouguer gravity anomaly in the eastern Tibetan Plateau and adjacent areas. Left: CEBG method (*a*); Right: SBG method (*b*).

and its adjacent areas. The values obtained by the above methods mainly vary between –600 and 150 mGal. The Bouguer gravity anomalies obtained by the CEBG and SBG methods were plotted with the same colour scale. The results indicate that the overall distributions of positive and negative Bouguer gravity anomalies are consistent, but the detailed distribution trends and data are quite different in areas. We further analysed the differences between the CEBG and SBG methods by taking the residual and the absolute value of the residual.

Figures 10 (a) and (b) show the distributions of the differences between the Bouguer gravity anomalies obtained by the different Bouguer gravity reduction methods (CEBG and SBG, respectively), as well as the absolute value of the differences. As shown in Figure 10a, the difference between the CEBG and SBG values mainly varies between –60 and 20 mGal, and the Bouguer gravity anomaly difference shows a gradually increasing trend from the southeast to the northwest of the study area. The absolute value of the difference between the CEBG and SBG methods mainly varies between 0 and 40 mGal (Fig. 10b). By superposing the absolute value of the difference between the CEBG and SBG methods, different colour points represent different levels of the absolute value of the difference; the result is projected onto the topographic map of the study area. The absolute value of the difference can be divided into four levels accord-
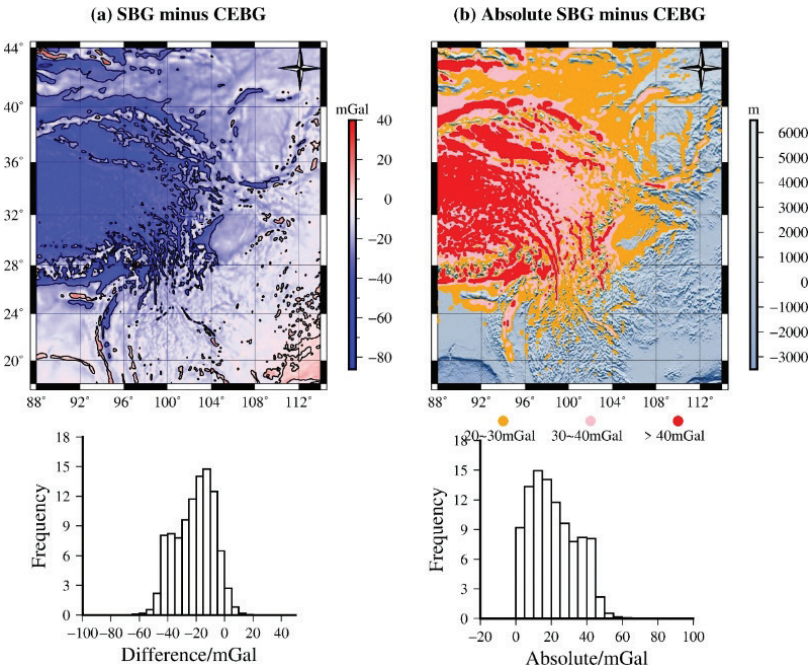


**Figure 10.** Difference between the SBG and CEBG methods. Left: SBG minus CEBG (*a*); Right: absolute SBG minus CEBG (*b*).

ing to the terrain variation within the study area. First, where the elevation is less than 1000 m, the absolute value of the difference is between 0 and 20 mGal. Second, where the elevation is between 1,000 m and 2,000 m, the absolute value of the difference varies between 20 and 30 mGal. Third, where the elevation is between 3,000 m and 5,000 m, the absolute value of the difference is between 30 and 40 mGal. Fourth, where the elevation is more than 5,000 m, the absolute value of the difference varies between 40 and 60 mGal. Combined with Figs. 9 and 10, it can be seen that the greater the elevation is, the greater the difference between the CEBG and SBG values.

### 4.3. Comparison of the interface inversion results with the different Bouguer reduction methods

Satellite gravity data are characterized by high coverage, high precision, and high spatial resolution and are widely used to study the spatial distribution of deep subsurface geological bodies and interfaces. The Moho is the interface between the lower crust and the upper mantle and represents a dynamic interface of material exchange and energy exchange between the crust and mantle. The Studying the fluctuation of the Moho is of valuable significance to understanding the formation and evolution of the crust and mantle and the dynamics of the deep Earth (Teng, 2006).

Data from the basis of geophysical forward inversion and interpretation. The results obtained by inversion with different data but the same method may be quite different from the final interpretation results. As mentioned above, the Bouguer gravity anomalies derived from satellite gravity data based on the CBG, CEBG, and SBG correction methods are quite different from each other. Through an interface inversion of the Bouguer gravity anomalies obtained by these three different Bouguer gravity correction methods, we analysed the differences in Moho depths results obtained by the inversion of different Bouguer gravity anomaly data and discussed the selection of correction methods for satellite gravity data on this basis.

For the interface inversion method, we adopted the Parker-Oldenburg interface inversion method to invert the Bouguer gravity anomaly data obtained by the three different Bouguer correction methods (Parker, 1973; Oldenburg, 1974). The inversion parameters are set as follows: the reference depth is 31 km, the density difference is 400 kg/m$^3$, and the iteration accuracy is 0.001 km. In the inversion process, if the error between the two iterations meets the accuracy, then the inversion stops, and the resulting data are output.

Figure 11 shows the depth distribution of the Moho in the study area obtained by the Bouguer gravity data inversion with the CBG (a), CEBG (b), and SBG (c) methods. The crustal thickness or Moho depth obtained by the three groups varies from 20 to 70 km, and the overall trends of the three groups are consistent. However, the local shape and depth of the Moho are quite different
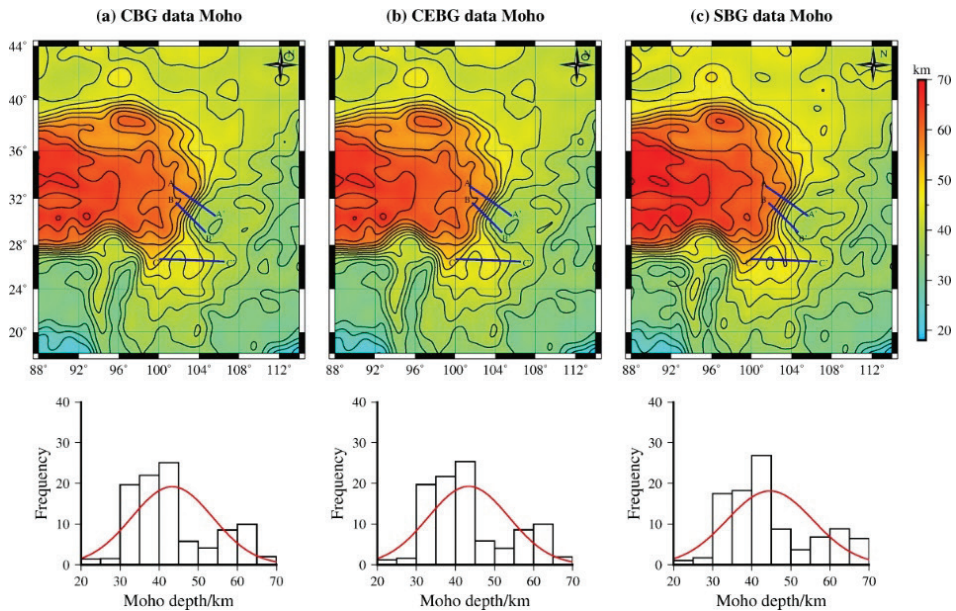
**Figure 11.** Moho depth map and histograms of the (*a*) CBG data, (*b*) CEBG data, (*c*) SBG data (blue line represent of real active seismic profiles).

among the three, especially between the SBG method and the other two Bouguer correction methods. To further analyse the differences in the Moho depth obtained from the three Bouguer gravity anomaly correction methods, the variations in the Moho depths obtained by the three different methods were obtained.
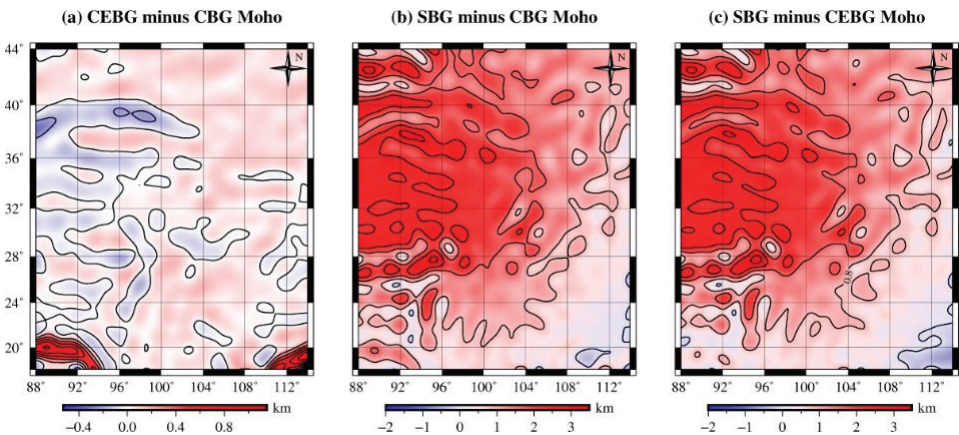


**Figure 12.** Moho differences between (*a*) CEBG minus CBG, (*b*) SBG minus CEBG, and (*c*) SBG minus CEBG.

*Table 1. Statistics of the differences between the Bouguer anomalies computed with CBG, CEBG, and SBG and their comparison. Unit: [km]*

| Differences | Max | Min | Mean | Median | Standard deviation |
|---|---|---|---|---|---|
| CEBG – CBG | 1.1506 | −0.5299 | 0.04537 | 0.0409 | 0.1204 |
| SBG – CBG | 3.4934 | −0.6316 | 1.3193 | 1.2331 | 0.7501 |
| SBG – CEBG | 3.4878 | −0.6766 | 1.2734 | 1.1687 | 0.7832 |

Figure 12 and Tab. 1 show the result of the depth difference analysis of the Moho obtained by the CBG, CEBG, and SBG methods. The differences among the SBG, CBG, and CEBG methods are −0.6 ~ 3.5 km.
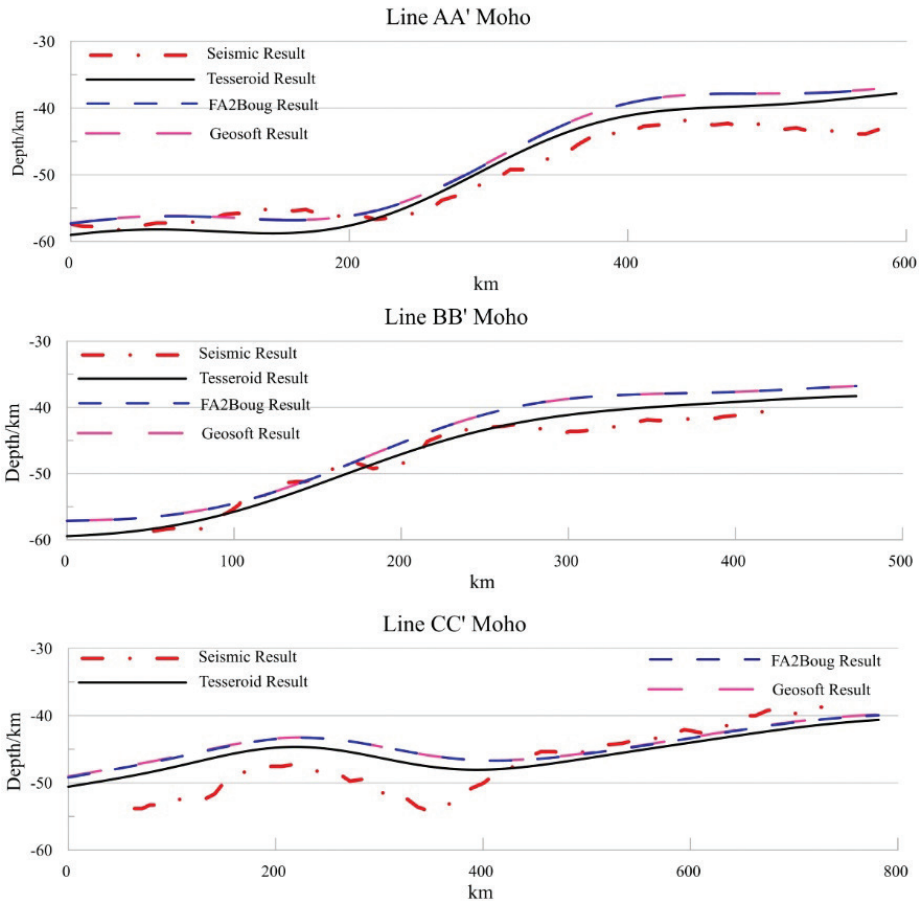


**Figure 13.** Comparison of the Moho depth results. *Top*: Section AA' ; *Middle*: Section BB'; *Bottom*: Section CC'.

To visually compare the results of the three different Bouguer correction methods regarding the inverted Moho, we collected the Moho depth results of from three active seismic profiles (Jia et al., 2014; Xu et al., 2015; Wang et al., 2015). Based on the Moho depth divided by the active seismic profile, the Moho surfaces obtained by the inversion of the Bouguer gravity anomaly data with the three different Bouguer correction methods were evaluated. The Moho surfaces obtained by the three different Bouguer correction methods were extracted and compared with the Moho profiles at the same location as the active seismic profiles (Fig. 13). Comparative analyses show that the results of the three Moho profiles with different Bouguer correction methods are consistent with the results of the active seismic profiles. Moreover, the profile depth changes obtained by the CBG and CEBG methods are almost identical, while the Moho depths from the SBG method are $2 \sim 3$ km deeper than those from the CBG and CEBG methods. This is consistent with the Bouguer gravity anomaly comparison among the CBG, CEBG, and SBG methods, and the overall trends of the three are consistent (Figs. 7 and 9). That is, the distributions of Bouguer gravity anomalies obtained by the CBG and CEBG methods are roughly the same, with only minor differences in the outliers. However, the differences between the in Bouguer gravity anomalies from the SBG and CEBG methods are significant in terms of both the anomaly distribution and the outliers. The Moho surface depths of the three different Bouguer correction methods and the Moho surface depths from the active seismic profiles were analysed comprehensively. The comparison indicates that the Moho depths obtained by the SBG method are closer to the active seismic profile results than those obtained by the other two Bouguer correction methods.

## 5. Conclusions

We took the eastern Tibetan Plateau and its adjacent areas (26°×26°) as the study area and conducted a comparative study on Bouguer gravity anomaly data obtained by the CBG, CEBG, and SBG correction methods. With increasing elevation, the calibrated gravitational effect affected by the curvature of the Earth will be grow. This indicates that the influence of the Earth's curvature on the gravitational effect cannot be ignored in the case of large terrain differences in the study range of 26°×26°.

Geophysical data form the prerequisite and necessary condition basis geophysical methods to carry out geological interpretation. In this paper, Moho depth maps were constructed with three different Bouguer correction methods and then compared and analysed against the Moho depths from active seismic profiles as a reference. The comparison shows that the transverse distribution trends of the Moho from the three different methods are consistent with those from the active seismic profiles, but there are some differences in the longitudinal distribution of the depth; the depth difference between the SBG method and the other two methods is $2 \sim 3$ km. A comprehensive comparison was performed

between the Moho depth from the three active seismic profiles and the Moho depths from the three Bouguer correction methods, indicating that the Moho depths obtained based on the Bouguer gravity anomaly data with the SBG method are closer to the measured results along the active seismic profiles.

Gravity data have the characteristics of a high horizontal resolution and low vertical resolution, and the depth of the Moho is one of the important outputs of longitudinal research employing gravity data. The lateral variations in the Moho depth obtained based on different Bouguer correction methods can reach up to 3 km. In applications to other extensive studies, such as the delineation of faults and identification of boundaries, this difference will be more noticeable when the Bouguer gravity anomalies obtained by different Bouguer correction methods are studied. The Moho depths from the SBG method are closer to the seismic profile results than the depths from the other two methods. Therefore, it is recommended that the SBG Bouguer correction method be adopted for global or regional gravity research, as it will produce results closer to the real situation.

# References

Almalki, K. A. and Mahmud, S. A. (2018): Gulfs of Suez and Aqaba: New insights from recent satellite-marine potential field data, *J. Afr. Earth Sci.*, **137**, 116–132, https://doi.org/10.1016/j.jafrearsci.2017.10.004.

Amante, C. and Eakins, B. W. (2009): ETOPO1 1 Arc-Minute global relief model: Procedures, data sources and analysis. *NOAA Technical Memorandum NESDIS NGDC-24.* National Geophysical Data Center, NOAA.

An, Y. L., Zhang, M. H., Huang, J. M. and Qiao, J. H. (2010): The computation scheme and computation process for gravity correction values with in the pure spherical coordinate system, *Geophysical And Geochemical Exploration*, **34**(6), 1–9 (in Chinese).

Asgharzadeh, M., Von Frese, R., Kim, H., Leftwich, T. and Kim, J. (2007): Spherical prism gravity effects by Gauss-Legendre quadrature integration, *Geophys. J. Int.*, **169**, 1–11, https://doi.org/10.1111/j.1365-246X.2007.03214.x.

Barthelmes, D. F. (2016): International Centre for Global Earth Models (ICGEM), available at: http://icgem.gfz-potsdam.de.

Bullard, E. C. (1936): Gravity measurements in east Africa, *Philos. Tr. Soc. S-A*, **235**(757), 445–531, https://doi.org/10.1098/rsta.1936.0008.

Chen, W., Tenzer, R. and Li, H. (2018): A regional gravimetric Moho recovery under Tibet using gravitational potential data from a satellite global model, *Stud. Geophys. Geod.*, **62**, 624–647, https://doi.org/10.1007/s11200-017-0812-5.

Cheney, R. E., Douglas, B. C., Agreen, R. W., Miller, L., Porter, D. L. and Doyle, N. S. (1987): Geosat altimeter geophysical data record user handbook. *Technical Report.* National Geodetic Survey, Charting and Geodetic Services National Ocean Service, NOAA Rockville, MD 20852, USA, 29 pp.

Deng, X. L. and Shen, W. B. (2019): Topographic effects up to gravitational curvatures of tesseroids: A case study in China, *Stud. Geophys. Geod.*, **63**, 345–366, https://doi.org/10.1007/s11200-018-0772-4.

Drewes, H., Kuglitsch, F., Adám, J. and Rózsa, S. (2016): The geodesist's handbook 2016, *J. Geodesy*, **90**, 907–1205, https://doi.org/10.1007/s00190-016-0948-z.

Emishaw, L. and Abdelsalam, M. G. (2019): Development of late jurassic-early paleogene and neogene-quaternary rifts within the Turkana Depression, East Africa from satellite gravity data, *Tectonics*, **38**, 2358–2377, https://doi.org/10.1029/2018tc005389.

Förste, C., Bruinsma, S., Abrykosov, O., Flechtner, F., Marty, J. C., Lemoine, J. M., Dahle, C., Neumayer, K. H., Barthelmes, F., König, R. and Biancale, R. (2014): EIGEN-6C4 — The latest combined global gravity field model including GOCE data up to degree and order 1949 of GFZ Potsdam and GRGS Toulouse, *Geophys. Res. Abstr.*, **16**, EGU2014-3707, General Assembly European Geosciences Union, Vienna, Austria.

Fu, L. L., Christensen, E. J., Yamarone Jr., C. A., Lefebvre, M., Menard, Y., Dorrer, M. and P. Escudier (1994): TOPEX/POSEIDON mission overview, *J. Geophys. Res. - Oceans*, **99**, 24369–24381, https://doi.org/10.1029/94JC01761.

Fullea, J., Fernàndez, M. and Zeyen, H. (2008): FA2BOUG—A FORTRAN 90 code to compute Bouguer gravity anomalies from gridded free-air anomalies: Application to the Atlantic-Mediterranean transition zone, *Comput. Geosci.*, **34**, 1665–1681, https://doi.org/10.1016/j.cageo.2008.02.018.

Green, C. M., Fletcher, K. M. U., Cheyney, S., Dawson, G. J. and Campbell, S. J. (2019): Satellite gravity – Enhancements from new satellites and new altimeter technology, *Geophys. Prospect.*, **67**, 1611–1619, https://doi.org/10.1111/1365-2478.12697.

Grombein, T., Seitz, K. and Heck, B. (2013): Optimized formulas for the gravitational field of a tesseroid, *J. Geodesy*, **87**, 645–660, https://doi.org/10.1007/s00190-013-0636-1.

Haxby, W. (1985): *Gravity field of world's oceans (color map)*. Lamont Doherty Geological Observatory of Columbia Univ., Palisades, New York.

Hayford, J. F. and Bowie, W. (1912): The effect of topography and isostatic compensation upon the intensity of gravity, *US Coast and Geod. Surv., Spec. Publ.*, **10**, 132 pp.

Heiskanen, W. A. and Moritz, H. (1967): *Physical geodesy*. WH Freeman, San Francisco.

Heck, B. and Seitz, K. (2007): A comparison of the tesseroid, prism and point-mass approaches for mass reductions in gravity field modelling, *J. Geodesy*, **81**, 121–136, https://doi.org/10.1007/s00190-006-0094-0.

Hofmann-Wellenhof, B. and Moritz, H. (2006): *Physical geodesy*. Springer Science and Business Media, XVII, 403 pp.

Jia, S. X., Liu, B. J., Xu, Z. F., Liu, Z., Feng, S. Y., Zhang, J. S., Lin, J. Y., Tian, X. F., Liu, Q. X. and Guo, W. B. (2014): The crustal structures of the central Longmenshan along and its margins as related to the seismotectonics of the 2008 Wenchuan earthquake, *Sci. China Earth Sci.,* **57,** 777–790, https://doi.org/10.1007/s11430-013-4744-9.

Kane, M. (1962): A comprehensive system of terrain corrections using a digital computer, *Geophysics*, **27**, 455–462, https://doi.org/10.1190/1.1439044.

LaFehr, T. R. (1990): An exact solution for the gravity curvature (Bullard B) correction, *Geophysics*, **56**, 1178–1184, https://doi.org/10.1190/1.1443138.

Lambert, W. O. (1930): The reduction of observed values of gravity to sea level, *Bulletin Géodésique* (1922–1941), **26**, 107–181.

Li, Z., Hao, T. Y., Xu, Y. and Xu, Y. (2011): An efficient and adaptive approach for modeling gravity effects in spherical coordinates, *J. Appl. Geophys.*, **73**, 221–231, https://doi.org/10.1016/j.jappgeo.2011.01.004.

Mahatsente, R., Önal, G. and Cemen, I. (2018): Lithospheric structure and the isostatic state of Eastern Anatolia: Insight from gravity data modelling, *Lithosphere*, **10**, 279–290, https://doi.org/10.1130/l685.1.

Maurya, V. P., Fontes, S. L. and Laterra, E. F. (2017): A fast novel approch to locate continent-oceanic boundary over South American passive margin, in: *15th International Congress of the Brazilian Geophysical Society and EXPOGEF*, Rio de Janeiro, Brazil, 31 July – 3 August 2017, 1049–1053.

Mikuška, J., Pašteka, R. and Marušiak. I. (2006), Estimation of distant relief effect in gravimetry, *Geophysics*, **71**, J59–J69, https://doi.org/10.1190/1.2338333.

Nagy, D., Papp, G. and Benedek, J. (2000): The gravitational potential and its derivatives for the prism, *J. Geodesy*, **74**, 552–560, https://doi.org/10.1007/s001900000116.

Nagy, D. (1966): The gravitational attraction of a right rectangular prism, *Geophysics*, **31**, 362–371, https://doi.org/10.1190/1.1439779.

Oldenburg (1974): The inversion and interpretation of gravity anomalies, *Geophysics*, **39**, 536, https://doi.org/10.1190/1.1440444.

Pail, R., Goiginger, H., Schuh, W. D., Höck, E., Brockmann, J. M., Fecher, T., Gruber, T., Mayer-Gürr, T., Kusche, J., Jäggi, A. and D. Rieser (2010): Combined satellite gravity field model GOCO01S derived from GOCE and GRACE, *Geophys. Res. Lett.*, **37**, L20314, https://doi.org/10.1029/2010GL044906.

Pal, S. and Majumdar, T. (2015): Geological appraisal over the Singhbhum-Orissa Craton, India using GOCE, EIGEN6-C2 and *in situ* gravity data, *Int. J. Appl. Earth Obs.*, **35**, 96–119, https://doi.org/10.1016/j.jag.2014.06.007.

Pappa, F., Ebbing, J. and Ferraccioli, F. (2019): Moho depths of Antarctica: Comparison of seismic, gravity, and isostatic results, *Geochem. Geophys. Geosy.*, **20**, 1629–1645, https://doi.org/10.1029/2018gc008111.

Parker, R. L. (1973): The rapid calculation of potential anomalies, *Geophys. J. Roy. Astr. S.*, **31**, 447–455, https://doi.org/10.1111/j.1365-246X.1973.tb06513.x.

Pastorutti, A. and Braitenberg, C. (2019): A geothermal application for GOCE satellite gravity data: Modelling the crustal heat production and lithospheric temperature field in Central Europe, *Geophys. J. Int.*, **219**, 1008–1031, https://doi.org/10.1093/gji/ggz344.

Pavlis, N. K., Holmes, S. A., Kenyon, S. C. and Factor, J. K. (2012): The development and evaluation of the Earth Gravitational Model 2008 (EGM2008), *J. Geophys. Res. – S. Ea.*, **117**(B4), https://doi.org/10.1029/2011JB008916.

Peters, M., Jung, W. and Brozena, J. (2018): Implication of gravity anomalies for lithospheric structure beneath Taiwan and its vicinity, *AGU Fall Meeting 2018*, Abstract #G51E-0521.

Rani, K., Guha, A., Mondal, S., Pal, S. K. and Vinod Kumar, K. (2019): ASTER multispectral bands, ground magnetic data, ground spectroscopy and space based EIGEN6C4 gravity data model for identifying potential zones for gold sulphide mineralization in Bhukia, Rajasthan, India, *J. Appl. Geophys.*, **160**, 28–46, https://doi.org/10.1016/j.jappgeo.2018.10.001.

Rathnayake, S., Tenzer, R., Eshagh, M. and Pitoňák, M. (2019): Gravity maps of the lithospheric structure beneath the Indian Ocean, *Surv. Geophys.*, **40**, 1055–1093, https://doi.org/10.1007/s10712-019-09564-6.

Rathnayake, S. and Tenzer, R. (2019): Interpretation of the lithospheric structure beneath the Indian Ocean from gravity gradient data, *J. Asian Earth Sci.*, **183**, 103934, https://doi.org/10.1016/j.jseaes.2019.103934.

Rignot, E. J., and Van Zyl, J. J. (1993): Change detection techniques for ERS-1 SAR data, *IEEE T. Geosci. Remote*, **31**, 896–906, https://doi.org/10.1109/36.239913.

Sobh, M., Ebbing, J., Götze, H. J. and Abdelsalam, M. (2018): The lithospheric structure of the Saharan Metacraton from 3D integrated geophysical-petrological modelling, CAU, https://doi.org/10.13140/RG.2.2.28688.71682.

Swick, C. H. (1942): Pendulum gravity measurements and isostatic reductions, *US Coast and Geod. Surv., Spec. Publ.*, **232**, 82.

Tamay, J., Galindo, Zaldivar, J., Martos, Y. and Soto, J. (2018): Gravity and magnetic anomalies of Ecuadorian margin: Implications in the deep structure of the subduction of Nazca Plate and Andes Cordillera, *J. S. Am. Earth Sci.*, **85**, 68–80, https://doi.org/10.1016/j.jsames.2018.04.020.

Teng, J. W. (2006): Research on layer-bundle fine structures and physical attributes of crust-mantle boundary in deep Earth, *Journal of Jilin University (Earth Science Edition)*, **36**, 1–23 (in Chinese).

Uieda, L., Barbosa, V. C. and Braitenberg, C. (2016): Tesseroids: Forward-modeling gravitational fields in spherical coordinates, *Geophysics*, **81**, F41–F48, https://doi.org/10.1190/geo2015-0204.1.

Vaish, J., and Pal, S. (2015): Geological mapping of Jharia Coalfield, India using GRACE EGM2008 gravity data: A vertical derivative approach, *Geocarto Internat.*, **30**, 388–401, https://doi.org/10.1080/10106049.2014.905637.

Wang, S. J., Wang, F. Y., Zhang, J. S., Liu, B. F., Zhang, C. K., Zhao, J. R., Duan, Y. L., Song, X. H., Deng, X. G., Ma, C. J. Sun, Y. N., Zang, Y. R. and Li, Y. Q. (2015): The deep seismogenic environment of Lushan Ms7.0 earthquake zone revealed by a wide-angle reflection/refraction seismic profile, *Chinese J. Geophys*, **58**, 3193–3204, https://doi.org/10.6038/cjg20150915.

Whitman, W. W. (1991): A microgal approximation for the Bullard B-earth's curvature-gravity correction, *Geophysics*, **56**, 1980–1985, https://doi.org/10.1190/1.1443009.

Wild-Pfeiffer, F. (2008): A comparison of different mass elements for use in gravity gradiometry, *J. Geod.*, **82**, 637–653, https://doi.org/10.1007/s00190-008-0219-8.

Xu, X., Ding, Z., Shi, D. and Li, X. (2013): Receiver function analysis of crustal structure beneath the eastern Tibetan plateau, *J. Asian Earth Sci.*, **73**, 121–127, https://doi.org/10.1016/j.jseaes.2013.04.018.

Xu, T., Zhang, Z. J., Liu, B. F., Chen, B., Zhang, M. H., Tian, X. B., Xu, Yi. G. and Teng, J. W. (2015): Crustal velocity structure in the Emeishan large igneous province and evidence of the Permian mantle plume activity, *Sci. China Earth Sci.*, **58**, 1133–1147, https://doi.org/10.1007/s11430-015-5094-6.

Xu, Z. P., Wang, F. Y., Jiang, L., Xu, S. L. and Tang, L. (2018): The depth of moho interface and crustal thickness in Sichuan-Yunnan region, *China Geology*, **40**, 1318–1331 (in Chinese), https://doi.org/10.3969/j.issn.0253-4967.2018.06.009.

Zhao, G., Chen, B., Uieda, L., Liu, J., Kaban, M. K., Chen, L. and Guo, R. (2019): Efficient 3-D large scale forward modeling and inversion of gravitational fields in spherical coordinates with application to lunar mascons, *J. Geophys. Res. - Sol. Ea.*, **124**, 4157–4173, https://doi.org/10.1029/2019jb017691.

Zhu, S. and Li, C. (2018): Effective elastic thickness of the North Atlantic lithosphere, AGU Fall Meeting.

SAŽETAK

## Usporedba različitih pristupa Bouguer-ove redukcije na temelju satelitskih gravimetrijskih podataka: primjer s Istočno-tibetanske visoravni i susjednih područja

*Fan Luo, Jiayong Yan, Kun Zhang, Chong Zhang, Guangming Fu i Xin Tao*

Gravimetrijski satelitski podaci u širokoj su primjeni u geofizici u proučavanju dubokih struktura na regionalnoj i globalnoj razini. Ti podaci uključuju i gravitacijske anomalije slobodnog zraka, koje obično treba korigirati na Bouguer-ovu gravitacijsku anomaliju, radi praktične primjene. Metode Bouguer-ove redukcije mogu se podijeliti u dvije skupine ovisno o primijenjenom koordinatnom sustavu: 1. metoda sfernih koordinata (SBG) i 2. metoda kartezijevih koordinata; potonja se dalje dijeli na metode CEBG i CBG, koje uključuju, odnosno ne uključuju korekciju zbog zakrivljenosti Zemlje. U ovom su radu

podaci o gravitacijskim anomalijama slobodnog zraka s Istočno-tibetanske visoravni i susjednih područja korišteni kao ulazni podaci za usporedbu triju metoda Bouguer-ove korekcije gravitacije: CBG, CEBG i SBG. Usporedba ove tri Bouguer-ove metode za gravitacijsku korekciju pokazala je da u istraživanom području učinak zakrivljenosti Zemlje na gravitaciju raste s povećanjem nadmorske visine. Cilj je bio shvatiti točnost inverzije za podatke dobivene različitim pristupima Bouguer-ovim anomalijama gravitacije. Raspodjele dubine Mohorovičićevog diskontinuiteta dobiveni su inverzijom Bouguer-ovih gravitacijskih anomalija dobivenih primjenom CBG, CEBG i SBG metoda, a aktivni seizmički profili korišteni su kao reference za usporedbu i ocjenu. Rezultati pokazuju da se dubine Mohorovičićevog diskontinuiteta dobivene SBG inverzijom bolje podudaraju s izmjerenim dubinama na seizmičkom profilu. Stoga se SBG metoda preporučuje kao najrealističniji pristup u postupku globalnih ili regionalnih istraživanja koja koriste gravimetrijske podatke.

*Ključne riječi*: pristup Bouguer-ove redukcije, sferne koordinate, Mohorovičićev diskontinuitet, Istočno-tibetanska visoravan i susjedna područja

*Corresponding author's address*: Jiayong Yan, Chinese Academy of Geological Sciences, 26 Baiwanzhuang Street, Xicheng District, Beijing, China; tel: +86 135 5235 0590; e-mail: yanjy@163.com (ORCID:0000-0002-7787-5572).